

Article

The Hybrid FEM-DBCI for the Solution of Open-Boundary Low-Frequency Problems

Giovanni Aiello, Salvatore Alfonzetti *, Santi Agatino Rizzo  and Nunzio Salerno 

Dipartimento di Ingegneria Elettrica, Elettronica e Informatica (DIEEI), Università di Catania, Viale A. Doria, 6, I-95125 Catania, Italy; giovanni.aiello@dieei.unict.it (G.A.); santi.rizzo@unict.it (S.A.R.); nunzio.salerno@unict.it (N.S.)

* Correspondence: alfo@dieei.unict.it; Tel.: +39-095-738-2320; Fax: +39-095-330-793

Abstract: This paper describes a particular use of the hybrid FEM-DBCI, for the computation of low-frequency electromagnetic fields in open-boundary domains. Once the unbounded free space enclosing the system has been truncated, the FEM is applied to the bounded domain thus obtained, assuming an unknown Dirichlet condition on the truncation boundary. An integral equation is used to express this boundary condition in which the integration surface is selected in the middle of the most external layer of finite elements, very close to the truncation boundary, so that the integral equation becomes quasi-singular. The method is described for the computation of electrostatic fields in 3D and of eddy currents in 2D, but it is also applicable to the solution of other kinds of electromagnetic problems. Comparisons are made with other methods, concluding that FEM-DBCI is competitive with the well-known FEM-BEM and coordinate transformations for what concerns accuracy and computing time.

Keywords: finite element method; integral equations; open-boundary problems; electrostatics; skin effect; GMRES



Citation: Aiello, G.; Alfonzetti, S.; Rizzo, S.A.; Salerno, N. The Hybrid FEM-DBCI for the Solution of Open-Boundary Low-Frequency Problems. *Mathematics* **2021**, *9*, 1968. <https://doi.org/10.3390/math9161968>

Academic Editor: Jacques Lobry

Received: 21 June 2021

Accepted: 10 August 2021

Published: 17 August 2021

Publisher's Note: MDPI stays neutral with regard to jurisdictional claims in published maps and institutional affiliations.



Copyright: © 2021 by the authors. Licensee MDPI, Basel, Switzerland. This article is an open access article distributed under the terms and conditions of the Creative Commons Attribution (CC BY) license (<https://creativecommons.org/licenses/by/4.0/>).

1. Introduction

Computational electromagnetics (CEM) in industrial applications are continuously growing due to the increasing performances of electronic computers and to the development of several commercial codes based on the finite element method (FEM) [1,2], by means of which complex geometries and materials can be dealt with.

However, serious difficulties appear when the device to be analyzed exhibits electromagnetic fields extending to infinity. Unfortunately, these fields are highly common in several electromagnetic systems.

In order to apply FEM, the unlimited domain must be cut by means of a closed truncation boundary Γ_T . Once the interior bounded domain has been discretized by finite elements, a boundary condition must be imposed on such a boundary, which should be very close to the true one, which is clearly not known. The simplest way to overcome this difficulty is to place Γ_T far away from the system core and impose on it a homogeneous condition, very often of the Dirichlet type. This approach exhibits poor accuracy-computational effort ratios, especially in the optimized design of three-dimensional electromagnetic devices.

For this reason, several specific methods have been devised to make the FEM able to compute scalar and vector fields in unbounded domains in a more efficient way.

In almost all these methods, the unbounded domain is partitioned into two parts by means of a cutting closed surface Γ_T , in such a way that the interior domain is sufficiently small and encloses the core of the system, whereas the unbounded exterior domain is homogeneously constituted of free space.

The interior domain is analyzed by means of the FEM, whereas for the exterior one several auxiliary methods have been devised in the literature, starting from the 1970s [3].

The research is still continuing, especially toward methods appropriate to the design optimization, which very often requires thousands of analyses and, therefore, short computing times to be effective.

In the CEM scenario, these auxiliary methods vary notably from low frequency (LF) to high frequency (HF) applications. For LF problems, we mention the coordinate transformations (CT) [4,5], infinite elements [6] and asymptotic boundary conditions (LF-ABC) [7], whereas for HF problems we mention the absorbing boundary conditions (HF-ABC) [8,9], and the perfectly matched layer (PML) [10].

All the methods mentioned above have the merit of leading to sparse algebraic systems, but they have the disadvantage of requiring a connected and convex truncation boundary. Then, these methods are not efficient when the system consists of several objects distributed in space, since a large free space must be meshed.

In these cases, hybrid methods are more suitable. The term hybrid comes from the fact that an integral equation (IE) is coupled with a partial differential equation (PDE) for the interior domain. The PDE is numerically treated by means of the FEM, whereas the IE is used to express the unknown boundary condition on the truncation surface Γ_T , which now can be constituted by several closed surfaces in such a way to minimize the meshing of the free space (domain decomposition). These methods are collectively called FEM-IE.

By considering that the boundary conditions on Γ_T can be of three types, namely Dirichlet, Neumann and Robin, and that the surface Γ_{IE} , support of the integral equation, may coincide or may not with Γ_T , theoretically we can have six hybrid methods. Table 1 reports some of these methods. Here again we observe two scenarios for LF and HF problems. For LF problems, we mention the FEM-DBCI (Dirichlet boundary condition iteration) [11–16], the FEM-SDBCI (singular DBCI) [17,18] and the well-known FEM-BEM [19,20], whereas for HF problems the FEM-MoM (Method of moments) [21], FEM-RBCI (Robin boundary condition iteration) [22,23], the FEM SRBCI (singular RBCI) [24] and the FEM-AABC (adaptive absorbing boundary condition) [25].

Table 1. Various FEM-IE methods.

| | Dirichlet | Neumann | Robin |
|-------------------------------|-------------------|---------------------------------|------------------------------|
| $\Gamma_T \neq \Gamma_{IE}$ | FEM-DBCI (LF) | – | FEM-RBCI FEM-AABC (HF) |
| $\Gamma_T \equiv \Gamma_{IE}$ | FEM-SDBCI (LF) | FEM-BEM FEM-MoM (LF) (HF) | FEM-SRBCI (HF) |

The use of Dirichlet or Neumann conditions on Γ_T for HF problems may give rise to internal resonances [2], so that these boundary conditions are not recommended, even if in particular cases the relative methods may work correctly. On the contrary, the use of a suitable Robin boundary condition avoids completely the internal resonances, whatever the frequency [22].

The BCI acronym to designate some of the hybrid methods in Table 1 comes from a particular solving iterative procedure, devised by the authors and reported in Section 4 for readers’ convenience. Note that this procedure is fully applicable also to FEM-BEM algebraic systems.

In this paper, we are focused on the FEM-DBCI method for LF problems. The truncation boundary Γ_T is selected by the user in such a way to enclose all the conductors and non-homogeneous objects and to truncate the unbounded free space around the system. On this boundary, a Dirichlet condition is assumed and initially guessed in order to obtain a first solution by means of standard FEM. An improvement of the Dirichlet condition on Γ_T can be obtained starting from this solution, by means of an integral equation, whose support is another closed surface Γ_{IE} , enclosing the system but strictly enclosed by Γ_T . This procedure is repeated iteratively until convergence is reached. A geometrically simple

Γ_{IE} is obtained in 3D as a set of triangular or quadrangular faces of internal tetrahedra or bricks, respectively, or as set of segments which are sides of triangles or quadrangles in 2D.

This paper describes a particular use of the FEM-DBCI method in which the integration surface is selected as constituted by patches connecting the middle points of the edges leaving from the truncation boundary Γ_T . In this way, the free space between Γ_{IE} and Γ_T reduces to half a layer of finite elements and, due to the proximity of Γ_{IE} and Γ_T , the integral equation becomes quasi-singular.

The paper is organized as follows: in Sections 2 and 3, the FEM-DBCI formulations are described for an electrostatic problem in 3D and for a time-harmonic skin effect problem in 2D, respectively. In Section 4, various algorithms to solve the hybrid global algebraic system are outlined. In Sections 5 and 6, analytical and numerical examples are given, respectively. The authors' conclusions follow in Section 7.

2. The FEM-DBCI Method for Electrostatics

Consider an electrostatic system constituted by dielectric objects, charge distributions and voltaged conductors embedded in free space, as shown in Figure 1. The conductor potentials $V_i, i = 1, \dots, N_C$, are relative to the zero potential at infinity.

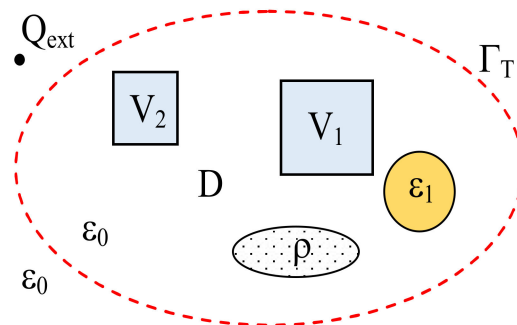


Figure 1. Fictitious boundary enclosing an electrostatic system of voltaged conductors, non-homogeneous dielectric objects and distributed sources.

In order to apply the FEM, a fictitious truncation boundary Γ_T is introduced in such a way to enclose all the conductors and non-homogeneous objects. Some lumped or distributed charges may be left out. In the bounded domain D , the Poisson equation holds [1]:

$$-\epsilon_0 \nabla \cdot (\epsilon_r \nabla v) = \rho \tag{1}$$

where ϵ_0 is the vacuum electric permittivity, ϵ_r is the relative permittivity, v is the electric scalar potential and ρ is the charge density. An unknown Dirichlet condition is assumed on Γ_T .

By meshing the domain D by means of nodal finite elements and applying the FEM, the following algebraic system is derived [11]:

$$\mathbf{M}v = \mathbf{k}_0 - \mathbf{M}_T v_T \tag{2}$$

where v and v_T are the arrays of the nodal values of the potential $v(x,y,z)$ at the internal nodes and at the nodes lying on Γ_T , respectively, \mathbf{M} and \mathbf{M}_T are sparse matrices of coefficients depending on geometry and materials and \mathbf{k}_0 is the known term array due to the conductor voltages and internal sources.

The Dirichlet condition on Γ_T is expressed by means of the integral equation:

$$v(\mathbf{r}) = v_{\text{ext}}(\mathbf{r}) + \int_{\Gamma_{IE}} \left(v(\mathbf{r}') \frac{\partial G(\mathbf{r}, \mathbf{r}')}{\partial n'} - G(\mathbf{r}, \mathbf{r}') \frac{\partial v(\mathbf{r}')}{\partial n'} \right) dS' \quad \mathbf{r} \in \Gamma_T \tag{3}$$

where v_{ext} is the potential due to the external sources, Γ_{IE} is the closed surface which connect the middle points of the edges leaving the nodes of Γ_{T} , as shown in Figure 2, \mathbf{n}' is the outward normal unit vector and G is the free-space Green's function:

$$G(\mathbf{r}, \mathbf{r}') = \frac{1}{4\pi|\mathbf{r} - \mathbf{r}'|} \tag{4}$$

Note that Equation (3) is valid if the space outside Γ_{IE} consists of free-space only. In numerical form, Equation (3) reads

$$v_i = v_{\text{ext}}(\mathbf{r}_i) + \sum_k \sum_m v_m \left(\xi_{\text{im}}^{(k)} - \eta_{\text{im}}^{(k)} \right) \tag{5}$$

where:

$$\xi_{\text{im}}^{(k)} = \iint_{S_k} \alpha_m(\mathbf{r}') \frac{\partial G(\mathbf{r}_i, \mathbf{r}')}{\partial n'} ds' \tag{6}$$

$$\eta_{\text{im}}^{(k)} = \iint_{S_k} \frac{\partial \alpha_m(\mathbf{r}')}{\partial n'} G(\mathbf{r}_i, \mathbf{r}') ds' \tag{7}$$

where S_k is the k -th patch of Γ_{IE} , α_m is the shape function of the m -th node of the finite element in which the patch lies, \mathbf{r}_i is the coordinate vector of the i -th node on Γ_{T} and v_i is the potential value at this node. Note that the patches S_k , which constitute Γ_{IE} , are triangles and quadrangles for a tetrahedral mesh and quadrangles for bricks [26].

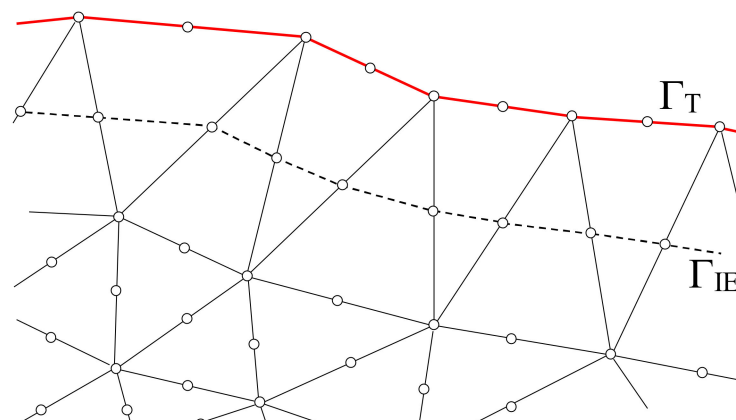


Figure 2. Truncation boundary Γ_{T} and integration curve Γ_{IE} (dashed line) in a mesh of triangular finite elements of the second order.

Since the patch S_k is detached from Γ_{T} , the integrals (6) and (7) are regular and can be computed by means of the Gauss quadrature with varying accuracy. When the centre of the integration patch S_k is far apart from the node \mathbf{r}_i on Γ_{T} , one-point Gauss quadrature is enough. When the centre of S_k is very close to \mathbf{r}_i , a large number of Gauss points are needed. Denoting by L the length of the longest edge of S_k and by d the distance of its centre from node \mathbf{r}_i on Γ_{T} , for first-order tetrahedra a good trade-off between accuracy and speed is the following: if $L/d < 0.2$ one-point Gauss is used; if $0.2 < L/d < 1.1$, three or four Gauss points are used for triangular or quadrangular patches, respectively; otherwise, six or nine points are used. If \mathbf{r}_i is very near to S_k , analytical formulas may be also used [27].

In matrix form, Equation (5) read:

$$\mathbf{H} \mathbf{v}_{\text{T}} = v_{\text{ext}} + \mathbf{G} \mathbf{v} \tag{8}$$

where matrices \mathbf{H} and \mathbf{G} are dense. \mathbf{H} is square by construction.

Equations (2) and (8) constitute the hybrid global algebraic system to be solved.

3. The FEM-DBCI Method for Skin Effect

The system considered consists of a set of N_C parallel straight conductors embedded in free space. We denote by S_k ($k = 1, \dots, N_C$) their cross sections and by I_k the phasors of the total currents, supposed to be time-harmonic of the same angular frequency ω . Each conductor is homogeneous, with reluctivity ν_k and conductivity σ_k . The current densities in these conductors are not known due to the skin and proximity effects.

Other conductors of small cross sections may exist carrying sinusoidal currents of the same angular frequency ω , represented by the phasors I_k , $k = N_{C+1}, \dots, N_{tot}$ (it is assumed that the sum of the currents of all the conductors be equal to zero). In these conductors the skin-effect is negligible, so that the current density is known and equal to I_k/S_k . From the point of view of the magnetic field, these conductors may or may not be homogeneous with the free space.

Now we truncate the unbounded free space by means of a fictitious boundary Γ_T , which must include all the skin-effect conductors and also the inhomogeneous skin-effect free ones. The skin-effect free conductors may be left outside Γ_T if magnetically homogeneous with free space. In the following, they are referred to as external sources.

The magnetic vector potential A is parallel to the conductor direction and in the k -th conductor satisfies the integro-differential equation [28]:

$$\nabla \cdot (\nu_k \nabla A) - j\omega\sigma_k A + j\omega I_k \frac{1}{S_k} \iint_{S_k} A \, dS = -\frac{I_k}{S_k} \quad \text{in } S_k \tag{9}$$

In the internal skin-effect free conductors, Equation (9) simplifies into the Poisson one, obtained by setting $\sigma_k = 0$ in it. In free space, the potential satisfies the Laplace equation.

Meshing the bounded domain by means of nodal finite elements and assuming a Dirichlet condition on Γ_T , the following matrix equation is obtained [14]:

$$\mathbf{M}\mathbf{a} = \mathbf{k}_0 - \mathbf{M}_T \mathbf{a}_T \tag{10}$$

where \mathbf{a} and \mathbf{a}_T are the arrays of the complex potential values of the magnetic vector potential at the internal and boundary nodes, respectively, \mathbf{M} is a square symmetric matrix which depends on geometry and materials, \mathbf{k}_0 is the known term array due to the internal source currents, and \mathbf{M}_T is a matrix of coefficients similar to \mathbf{M} .

Arrays \mathbf{a} and \mathbf{a}_T can be further related by means of the integral equation:

$$A(\mathbf{r}) = A_{\text{ext}}(\mathbf{r}) + \oint_{\Gamma_{IE}} \left(A(\mathbf{r}') \frac{\partial G(\mathbf{r}, \mathbf{r}')}{\partial n'} - G(\mathbf{r}, \mathbf{r}') \frac{\partial A(\mathbf{r}')}{\partial n'} \right) ds' \quad \mathbf{r} \in \Gamma_T \tag{11}$$

where A_{ext} is the potential due to the external source currents, if any, Γ_{IE} is the closed broken line which connect the middle points of the element sides leaving the nodes of Γ_T , and G is the two-dimensional free-space Green's function:

$$G(\mathbf{r}, \mathbf{r}') = -\frac{1}{2\pi} \ln |\mathbf{r} - \mathbf{r}'| \tag{12}$$

In the numerical approximation, Equation (11) reads:

$$\mathbf{H}\mathbf{a}_T = \mathbf{a}_{\text{ext}} + \mathbf{G}\mathbf{a} \tag{13}$$

where \mathbf{H} and \mathbf{G} are dense matrices of geometrical coefficients and \mathbf{a}_{ext} depends on the external sources. Matrix \mathbf{H} is square. Equations (10) and (13) constitute the global algebraic system to be solved.

4. Solution of the Global Algebraic System

In the FEM-DBCI methods described previously, the global algebraic systems have the forms

$$\begin{bmatrix} \mathbf{M} & \mathbf{M}_T \\ -\mathbf{G} & \mathbf{H} \end{bmatrix} \begin{bmatrix} \mathbf{x} \\ \mathbf{x}_T \end{bmatrix} = \begin{bmatrix} \mathbf{k}_0 \\ \mathbf{k}_{\text{ext}} \end{bmatrix} \tag{14}$$

where \mathbf{M} and \mathbf{M}_T are sparse matrices, \mathbf{H} and \mathbf{G} are dense matrices, \mathbf{x} and \mathbf{x}_T are unknown vectors relative to the FEM unknowns and to the truncation boundary condition unknowns, respectively, and \mathbf{k}_0 and \mathbf{k}_{ext} are known arrays. \mathbf{M} and \mathbf{H} are square.

System (14) can be solved by iteration. Starting from a first guess $\mathbf{x}_T^{(0)}$ for \mathbf{x}_T , the FEM equation is solved for $\mathbf{x}^{(0)}$; then, the integral equation is used to improve this guess. These two steps are iterated. At the generic p -th iteration step:

$$\mathbf{M}\mathbf{x}^{(p)} = \mathbf{k}_0 - \mathbf{M}_T\mathbf{x}_T^{(p)} \tag{15}$$

$$\mathbf{H}\mathbf{x}_T^{(p+1)} = \mathbf{k}_{\text{ext}} + \mathbf{G}\mathbf{x}^{(p)} \tag{16}$$

By considering the symmetry and sparsity of matrix \mathbf{M} , the algebraic system (15) is conveniently solved by means of the conjugate gradient (CG) solver [29]. System (16) may be solved by means of the LU factorization of matrix \mathbf{H} , which, however, is performed only once at the 0-th step.

The convergence behavior of this iterative procedure can be studied as follows. When systems (15) and (16) are solved, we obtain:

$$\mathbf{x}_T^{(p+1)} = \mathbf{p}_0 + \mathbf{P}\mathbf{x}_T^{(p)} \tag{17}$$

where:

$$\mathbf{p}_0 = \mathbf{H}^{-1}(\mathbf{k}_{\text{ext}} + \mathbf{G}\mathbf{M}^{-1}\mathbf{k}_0) \tag{18}$$

$$\mathbf{P} = -\mathbf{H}^{-1}\mathbf{G}\mathbf{M}^{-1}\mathbf{M}_T \tag{19}$$

The step matrix \mathbf{P} determines the convergence of the iterative procedure. In fact, if its spectral radius ρ is lower than 1, convergence is obtained to the true solution of the unbounded problem whatever the initial guess $\mathbf{x}_T^{(0)}$. In [30], it is shown that the condition $\rho < 1$ is satisfied if the mean distance of Γ_T from the conductors is greater than the mean radius of the conductor system.

If relaxation is used, the step Equation (17) changes into:

$$\mathbf{x}_T^{(p+1)} = \lambda\mathbf{p}_0 + [(1 - \lambda)\mathbf{I} + \lambda\mathbf{P}]\mathbf{x}_T^{(p)} \tag{20}$$

With a suitable value of the relaxation parameter λ , the iterative procedure converges even when the non-relaxed procedure does not [31]. Unfortunately, only heuristic rules have been derived for setting λ , so that this approach is not satisfactory.

By looking at the iterative algorithm more deeply, it is simple to realize that Equations (17) and (20) can be seen as the iterative relations to solve the reduced algebraic systems:

$$(\mathbf{I} - \mathbf{P})\mathbf{x}_T = \mathbf{p}_0 \quad \lambda(\mathbf{I} - \mathbf{P})\mathbf{x}_T = \lambda\mathbf{p}_0 \tag{21}$$

respectively, by means of Richardson’s method [29], which is a weak and possibly non-converging solver.

In order to find a more efficient solver, we consider the reduced system:

$$\mathbf{A}\mathbf{x}_T = \mathbf{b} \tag{22}$$

where:

$$\mathbf{b} = \mathbf{k}_{\text{ext}} + \mathbf{G}\mathbf{M}^{-1}\mathbf{k}_0 \tag{23}$$

$$\mathbf{A} = \mathbf{H} + \mathbf{GM}^{-1}\mathbf{M}_T \tag{24}$$

Obviously, due to the impossibility to obtain the inverse matrix \mathbf{M}^{-1} , matrix \mathbf{A} and vector \mathbf{b} are not available directly. However, it is still possible to obtain \mathbf{b} in a simple way and to use matrix \mathbf{A} to perform matrix-vector multiplications. In fact, vector \mathbf{b} is obtained as follows:

- (1) Set a zero initial guess $\mathbf{x}_T^{(0)} = 0$ for the Dirichlet condition on Γ_T ;
- (2) Solve the FEM equation (by means of the CG) to find $\mathbf{x}^{(0)} = \mathbf{M}^{-1}\mathbf{k}_0$;
- (3) Compute $\mathbf{b} = \mathbf{k}_{\text{ext}} + \mathbf{G}\mathbf{x}^{(0)} = \mathbf{k}_{\text{ext}} + \mathbf{GM}^{-1}\mathbf{k}_0$.

In a similar way, matrix \mathbf{A} can be used to multiply it by an array $\mathbf{x}_T^{(p)}$:

- (a) Given the array $\mathbf{x}_T^{(p)}$;
- (b) Solve the FEM equation with $\mathbf{k}_0 = \mathbf{0}$ (by means of the CG) to find $\mathbf{x}^{(p)} = -\mathbf{M}^{-1}\mathbf{M}_T\mathbf{x}_T^{(p)}$;
- (c) Compute $\mathbf{A}\mathbf{x}_T^{(p)} = \mathbf{H}\mathbf{x}_T^{(p)} - \mathbf{G}\mathbf{x}^{(p)}$.

Then, we can solve system (22) by means of a variety of non-stationary CG-like solvers for non-symmetric matrices [29]. Among these, GMRES [32] should be preferred, as it really minimizes the number of matrix-by-vector multiplications, which are highly expensive in this context. As it is well known, the greater drawbacks of GMRES are the CPU time and the memory amount required to build and store the orthonormal base. However, in this application of GMRES, these requirements are moderately low, since GMRES virtually acts on a small system, whose unknowns are the potential values at the nodes of the truncation boundary [33].

This virtual use of the GMRES is fully applicable also to the solution of FEM-BEM algebraic systems, as described in [34].

5. An Analytical Example

This example is a very simple one: a perfectly conducting sphere voltaged at V_0 , embedded in free space. The analytical solution is well known, but here numerical solutions will be considered, based on the FEM-DBCI method.

In order to do this, a spherical truncation boundary is introduced at a distance d from the conductor surface. By virtue of the radial symmetry, the analysis can be conveniently led in the one-dimensional domain $D = [R, R + d]$, where R is the radius of the spherical conductor. In D , the Laplace equation holds:

$$\frac{1}{r^2} \frac{\partial}{\partial r} \left(r^2 \frac{\partial v}{\partial r} \right) = 0 \tag{25}$$

with the relative boundary conditions.

The domain D is regularly meshed by means of N first-order segments of the same length d/N ; the total number of nodes is $N+1$; their abscissas are $r_i = R + id/N$, $i = 0, \dots, N$. By virtue of the FEM-DBCI, the following system of algebraic equations is obtained:

$$\text{FEM : } -a_i v_{i-1} + (a_i + a_{i+1}) v_i - a_{i+1} v_{i+1} = 0 \quad i = 1, \dots, N - 1 \tag{26}$$

$$\text{DBCI : } v_N = h (v_{N-1} - v_N) \tag{27}$$

subject to the Dirichlet boundary condition $v(R) = v_0 = V_0$.

The coefficients a_i are given by:

$$a_i = \frac{1}{3} \left(r_{i-1}^2 + r_{i-1} r_i + r_i^2 \right) \quad i = 1, \dots, N \tag{28}$$

whereas the coefficient h depends on the choice of Γ_{IE} . By selecting Γ_{IE} as the spherical surface of radius

$$R_{IE} = R + d - \frac{1}{2} \frac{d}{N} \tag{29}$$

in the middle of the last segment, the coefficient h is given by:

$$h = \frac{NR_{IE}^2}{(R + d)d} \tag{30}$$

By solving the FEM-DBCI system (26)–(27), we get the potential value on the fictitious boundary:

$$v_N = \frac{h}{h + a_N\lambda_N} V_0 \tag{31}$$

where:

$$\lambda_N = \sum_{i=1}^N \frac{1}{a_i} \tag{32}$$

In order to check the validity of the FEM-DBCI method, we define the error indicator:

$$\eta_N = 100 \frac{v_N - v(\mathbf{r}_N)}{v(\mathbf{r}_N)} \tag{33}$$

where $v(\mathbf{r}_N)$ is the exact value of the potential on the fictitious boundary:

$$v(\mathbf{r}_N) = \frac{1}{1 + \delta} V_0 \tag{34}$$

where δ is the normalized distance of the truncation boundary from the conductor surface:

$$\delta = \frac{d}{R} \tag{35}$$

By substituting (31) and (34) in (33), the error indicator reads:

$$\eta_N = 100 \frac{\delta - \delta_N}{1 + \delta_N} \tag{36}$$

where δ_N is a non-dimensional values given by:

$$\delta_N = \frac{a_N\lambda_N}{h} \tag{37}$$

Since it is possible to show that

$$\lim_{N \rightarrow \infty} \delta_N = \delta \tag{38}$$

we have also

$$\lim_{N \rightarrow \infty} \eta_N = 0 \tag{39}$$

and the numerical solution v_N tends to the exact one. This validates the proposed method.

To compare the accuracy of the FEM-DBCI with that of other methods, consider the following FEM-BEM global algebraic system:

$$\text{FEM : } -a_i v_{i-1} + (a_i + a_{i+1}) v_i - a_{i+1} v_{i+1} = 0 \quad i = 1, \dots, N - 1 \tag{40}$$

$$- a_N v_{N-1} + a_N v_N = \frac{d}{N} (R + d)^2 q_N \tag{41}$$

$$\text{BEM : } v_N = - (R + d) q_N \tag{42}$$

where q_N is the unknown value of the outward normal derivative of the potential on Γ_T . By solving the system (40)–(42) subject to the Dirichlet boundary condition $v_0 = V_0$, we obtain the numerical solution for v_N :

$$v'_N = \frac{1}{1 + \frac{d}{N}(R + d) \lambda_N} V_0 \tag{43}$$

so that the error indicator is:

$$\eta'_N = 100 \frac{v'_N - v(r_N)}{v(r_N)} = 100 \frac{\delta - \delta'_N}{1 + \delta'_N} \tag{44}$$

where:

$$\delta'_N = \frac{1}{N} R^2 (1 + \delta) \delta \lambda_N \tag{45}$$

In Figure 3, the behaviours of η_N and η'_N for a fixed number of finite elements $N = 10$ are plotted as a function of δ . Good accuracies are obtained with both the methods, but FEM-DBCI is a little bit more accurate than FEM-BEM. Analogous results are obtained by increasing the number of finite elements. For higher values of N , the two lines tends to coincide with the $\eta = 0$ line. Mathematically, this is exactly obtained for $N \rightarrow \infty$.

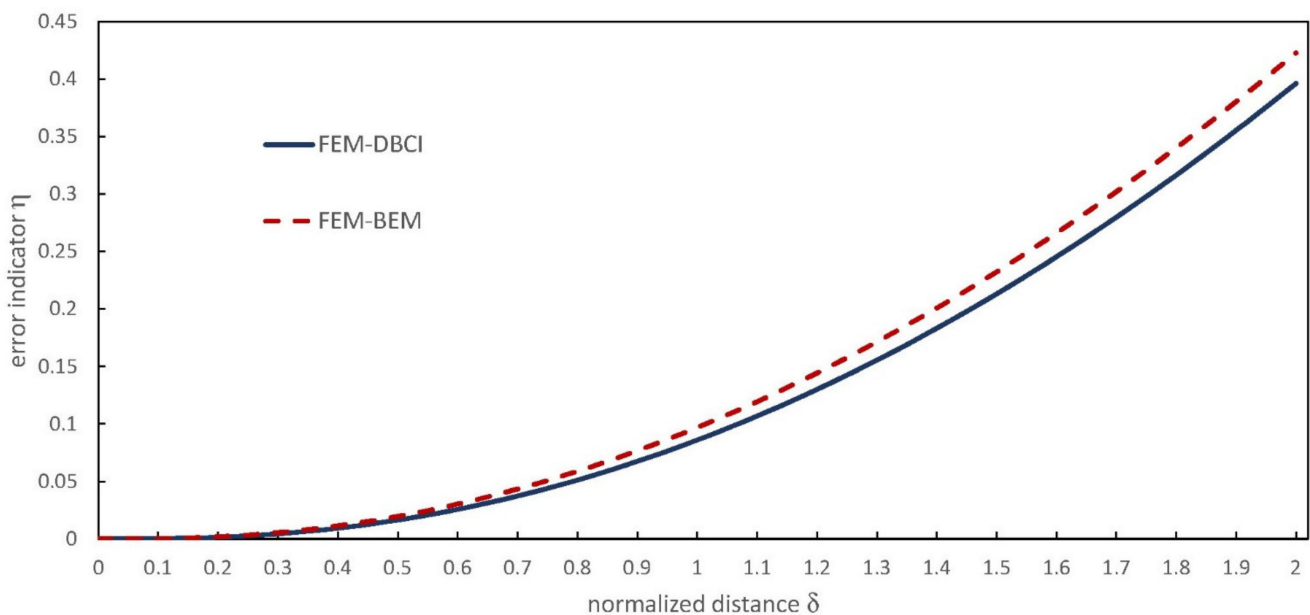


Figure 3. Behaviour of the error indicators of the FEM-DBCI and FEM-BEM methods for the analytical example of the charged conducting sphere.

However, in general, FEM-DBCI is a little bit less accurate than FEM-BEM, but much more fast since it works with a lower number of unknowns [35], the nodal values of the normal derivative of the potential not being used in the first one. This characteristic will be illustrated in the next section by means of a set of numerical examples.

6. Numerical Examples

6.1. Capacitance of a Strip Line

Consider the transmission line shown in Figure 4, where a conductor strip (width $w = 5$ mm, negligible thickness) is separated from a ground plane by a dielectric sheet (height $h = 1.5$ mm, width $s = 15$ mm, permittivity $\epsilon_1 = 4.7\epsilon_0$). The line is embedded in the free-space of permittivity ϵ_0 . The strip conductor is voltage at $V_0 = 1$ V. Due to symmetry reasons, the two-dimensional analysis can be restricted to half the system, by imposing

a homogeneous Neumann boundary condition on the y -axis. The truncation boundary is placed at a distance $d = 0.05$ mm from the conductor/dielectric, as shown in Figure 4. The mesh is formed with 1057 second-order triangles and 2240 nodes. Only one layer of 204 finite elements is in free-space; 206 nodes lie on Γ_T . The FEM-DBCI converges in six GMRES iterations, with an end-iteration tolerance of 0.01 per cent. The contours of the potential are shown in Figure 5. The capacitance per unit length is conveniently evaluated by means of the cross-energy formula:

$$c = \frac{2}{V_0} \iint_D \epsilon \nabla v \cdot \nabla w \, dx dy \tag{46}$$

where w is an arbitrary function such that $w = 1$ on the strip and $w = 0$ on the ground plane and on Γ_T . This computation gives: $c = 130.7$ pF/m.

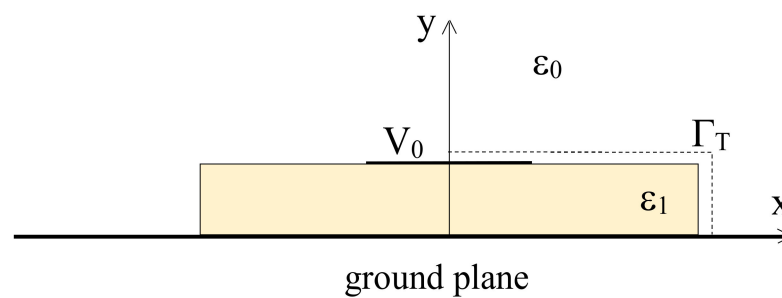


Figure 4. Microstrip line over a ground plane.

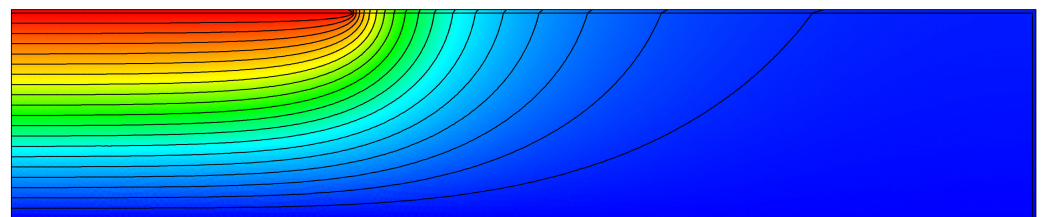


Figure 5. Contours of the electrical potential.

6.2. Two-Wire Transmission Line

The line considered is constituted by two circular wires of radius R whose centers are separated by a distance of $D = 2.4R$. The wire potentials are $V_0/2$ and $-V_0/2$, so that the analytical solution is [36]:

$$v^*(x, y) = \frac{V_0}{4 \cosh^{-1}(D/2R)} \ln \left[\frac{(x+a)^2 + y^2}{(x-a)^2 + y^2} \right] \tag{47}$$

where:

$$a = \sqrt{\frac{1}{4}D^2 - R^2} \tag{48}$$

and the capacitance per unit length is given by:

$$c = \frac{\pi \epsilon_0}{\cosh^{-1}(D/2R)} \tag{49}$$

For this line, Formula (49) gives $c = 5.047850 \epsilon_0$. The truncation boundary is selected as two circumferences of radius $1.14R$, concentric with the two wires. The air gap between the conductors and the truncation boundary Γ_T is $d = 0.14R$. Due to symmetry, the analysis can be conveniently limited to the first quadrant only, by imposing homogeneous Neumann and Dirichlet conditions on the x - and y -axis, respectively. Note that the y -axis is completely

left outside the domain of analysis. The air gap is regularly meshed with four layers of second-order triangular elements, for a total 724 elements and 1637 nodes. To improve the accuracy of the numerical solution, curved elements are used at the conductor-air interface. The integration curve Γ_{IE} is selected in three different ways: (a) triangle sides at a distance $d/4$ from the conductor; (b) segments internal to the 2nd layer of triangles at a mean distance of $3d/8$ from the conductor; (c) segments internal to the 4th layer of triangles at a mean distance of $7d/8$ from the conductor. Another analysis is performed by means of the non-standard FEM-BEM described in [20]. The various algebraic systems are solved with the GMRES schemes (restarting parameter $m = 10$). The following error indicator is employed to measure the accuracy of the numerical solutions:

$$\zeta = 100 \sqrt{\frac{\iint_{D_1} (v^* - v)^2 dx dy}{\iint_{D_1} (v^*)^2 dx dy}} \quad (50)$$

where D_1 is the analysis domain in the first quadrant. Table 2 summarizes the results obtained by reporting the number of steps performed (with an end-iteration tolerance of 10^{-3} per cent for the GMRES and for the CG), the normalized CPU time for the solution of the linear systems, the error indicators ζ and the normalized capacitances c/ϵ_0 , evaluated by means of the cross-energy formula. We can see that all the FEM-DBCI solutions are less accurate with respect to the FEM-BEM, but notably faster. Moreover, note the FEM-DBCI (c) solution is practically accurate as the (b) one, and this means that we can reduce the mesh to two layers only, by also reducing the relative CPU time.

Table 2. Comparison between various FEM-DBCI and FEM-BEM for the 2nd example.

| Method | GMRES Steps | CPU Time | Error Indicator ζ | Capacitance c/ϵ_0 |
|--------------|-------------|----------|-------------------------|----------------------------|
| FEM-DBCI (a) | 6 | 1.00 | 7.45×10^{-3} | 5.048423 |
| FEM-DBCI (b) | 6 | 1.02 | 6.71×10^{-3} | 5.047634 |
| FEM-DBCI (c) | 6 | 1.02 | 6.82×10^{-3} | 5.047570 |
| FEM-BEM | 8 | 2.01 | 2.19×10^{-3} | 5.047849 |

6.3. Capacitance of a Cube Conductor

The third example is relative to the computation of the capacitance C of a conductor cube of edge size s , voltage at V_0 and embedded in free space. For this classical three-dimensional electrostatic problem, a highly accurate estimate is known of the normalized capacitance $c = C/4\pi\epsilon_0 s$: $c = 0.6606780 \pm 2.7 \times 10^{-7}$ [37]. The FEM-DBCI method is applied by introducing a cube fictitious boundary Γ_T , placed homologously to the conductor surface at a distance $d = s/8$. This distance is justified by the need of spacing Γ_T from the cube edges, where the electrical field theoretically diverges. Thanks to symmetry, the analysis domain is limited to the first octant only. The free-space gap between the two cubes is meshed with 56,220 first-order tetrahedra with 11,948 nodes. Two estimates of the capacitance c are obtained by means of the FEM-DBCI and FEM-BEM. The number of GMRES steps (with an end-iteration tolerance of 10^{-2} per cent for the GMRES and 10^{-4} per cent for the CG), the CPU times for the solution of the linear algebraic systems and the normalized capacitances c are reported in Table 3. As before, FEM-DBCI exhibits an accuracy comparable with that of the FEM-BEM, but FEM-DBCI requires much less computing time. The contours of the potential are shown in Figure 6.

Table 3. Comparison between FEM-DBCI and FEM-BEM for the 3rd example.

| Method | GMRES Steps | CPU Time (ms) | Normalized Capacitance |
|----------|-------------|---------------|------------------------|
| FEM-DBCI | 4 | 161.7 | 0.662214 |
| FEM-BEM | 18 | 1421.9 | 0.661590 |

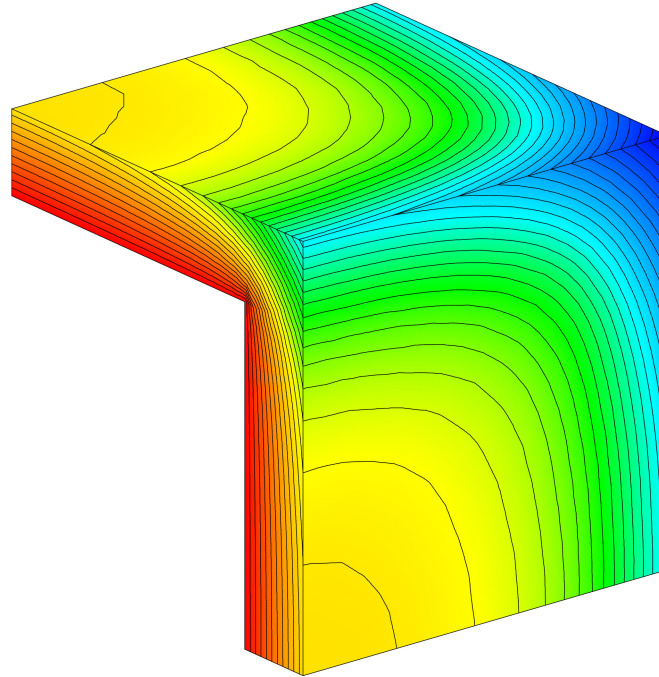


Figure 6. Contours of the potential around the cube conductor.

6.4. Skin Effect in a Two Wire Transmission Line

The transmission line is constituted by two conductors having circular cross-sections of radius $R = 5$ mm. The distance between the two centers is $D = 20$ mm (see Figure 7). The line carries two opposite sinusoidal currents of magnitude $I = 1$ A at frequency $f = 1$ kHz. The two wires are made of copper with conductivity $\sigma = 56 \times 10^6$ S/m. This example is given to compare FEM-DBCI with other methods: FEM truncation, FEM-CT (Coordinate Transformations) [4,5], and FEM-BEM.

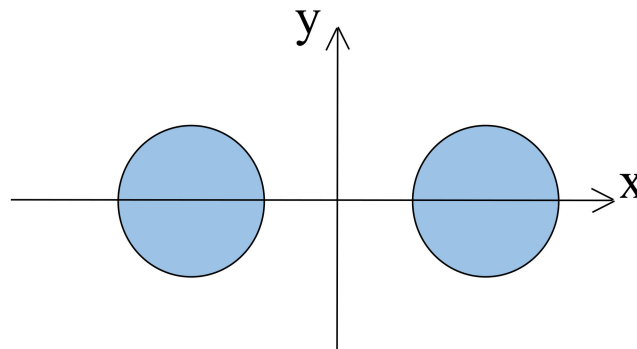


Figure 7. Two-wire transmission line.

By selecting the Cartesian reference frame in Figure 7, the transmission line exhibits a double symmetry with respect to the two axes, so that the various analyses can be restricted to the first quadrant only, by imposing a homogeneous Neumann condition on the x-axis and a homogeneous Dirichlet one on the y-axis.

Since no analytical solution exists for this problem, in the following we assume that the best solution be obtained by means of the FEM-CT method by employing a great radius of the circular domain $R_{CT} = 6 R = 30 \text{ mm}$ of the Kelvin transformation [4].

The interior domain is meshed with 370 triangular finite elements of the second order (see Figure 8). A total of 128 elements lay in the conductor; 242 elements lay in air (64 of which in the exterior air). The complex CG solver is used to solve the global algebraic system with a CPU time of $T_S = 0.26 \text{ s}$ on a small PC.

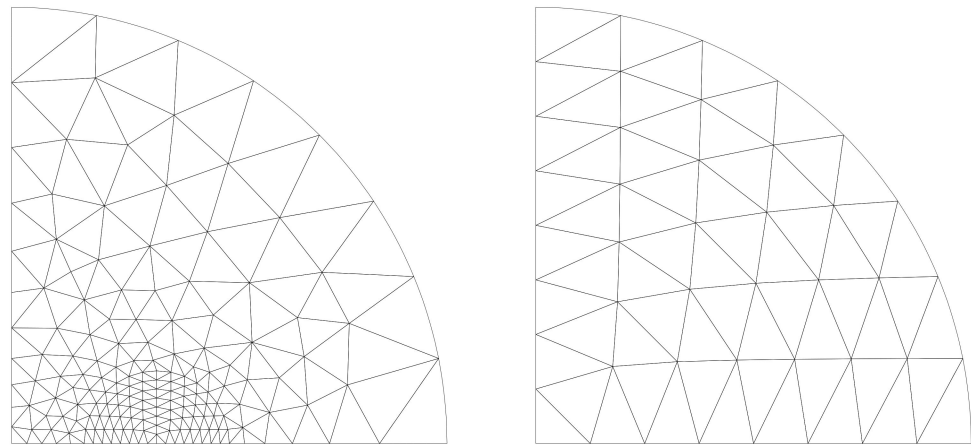


Figure 8. Finite element mesh in the interior and exterior regions in the FEM-CT analysis.

The FEM truncation method is then applied by means of a circular truncation boundary Γ_0 of radius R_0 , centered at the origin. On Γ_0 , a homogeneous Dirichlet condition is imposed. The radius of this circle is increased until a satisfactory accuracy is obtained with respect to the FEM-CT solution. To measure this accuracy, we use the following error indicator:

$$\eta = 100 \left(\frac{\iint_C |A^{(T)}(x, y) - A(x, y)|^2 dx dy}{\iint_C |A(x, y)|^2 dx dy} \right)^{\frac{1}{2}} \tag{51}$$

where A and $A^{(T)}$ are the FEM-CT and truncation solutions, respectively, and C denotes the conductor subdomain. Numerically, η is computed as:

$$\eta = 100 \left(\frac{\sum_{k \in C} \sum_n \sum_m t_{nm} \operatorname{Re} \left\{ (A_n^{(T)} - A_n) (A_m^{(T)} - A_m)^* \right\}}{\sum_{k \in C} \sum_n \sum_m t_{nm} \operatorname{Re} \left\{ A_n A_m^* \right\}} \right)^{\frac{1}{2}} \tag{52}$$

where n and m are indices of nodes in the k -th finite element (belonging to the conductor), star denotes conjugation and t_{nm} is an entry of the metric matrix of the k -th element [1]. We found that by setting $R_0 = 30 R$, the error indicator η decreases to 0.15% and the CPU increases to $1.90 T_S$.

The system is also analyzed by means of FEM-BEM. The air-copper interface is used as the truncation boundary. In the conductor, the mesh is formed with 128 second-order triangular finite elements, exactly coinciding with those of the previous analyses. The FEM-BEM system is solved by means of the GMRES solver, as explained in [15]. Solution is achieved in four iterations, but the CPU time rises to $1.52 T_S$, while the error indicator η decreases to 0.08%.

Finally, the FEM-DBCI method is applied by employing a circular truncation boundary of radius $R_T = 6.0 \text{ mm}$. The air in between the conductor and the truncation boundary is meshed by means of one layer of 32 triangular finite elements; the conductor is meshed as

in the previous analyses. The resulting global algebraic system is solved by means of the GMRES solver. The solution is reached in four iterations, with a CPU time of 1.14 T_S; the error indicator is 0.11%. Figure 9 reports the contours of the current density magnitude inside the conductor.

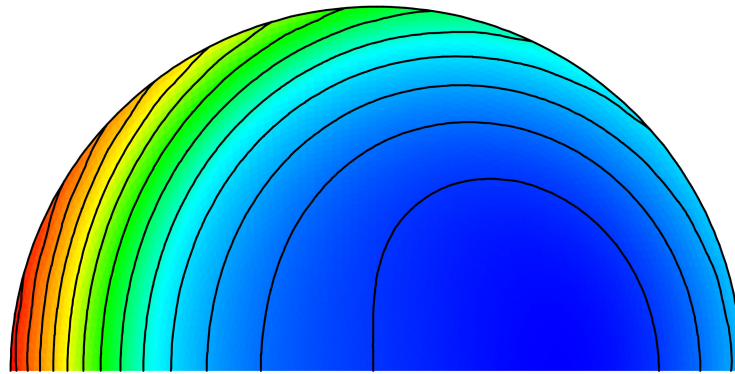


Figure 9. Contours of the current density magnitude.

The results obtained show that FEM-DBCI is competitive with respect to the well-known FEM-BEM and FEM-CT methods, both from the accuracy and CPU time points of view. Moreover, note that the FEM-BEM and FEM-DBCI performances can increase with respect to those of FEM-CT if the system analyzed consists of several conductors, the distances between which are much greater than their diameters.

6.5. Skin Effect in a Non-Symmetric Transmission Line

The last example concerns a non-symmetric transmission line constituted by a couple of conductors having different sections, as depicted in Figure 10. The geometrical data are: left conductor Section 1 cm × 1 cm, right conductor Section 2 cm × 2 cm, distance between their centres 2.3 cm. The conductors are made of copper ($\sigma = 56 \times 10^6$ S/m), whereas the surrounding medium is assumed to have zero conductivity and vacuum permeability. The conductors carry two opposite time-harmonic currents I and $-I$ of magnitude 1 A at frequency $f = 1$ kHz.

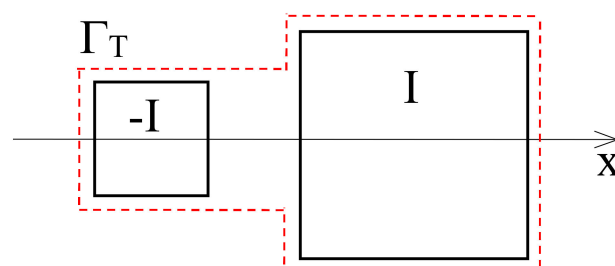


Figure 10. Non-symmetric two-wire transmission line.

This example is selected to show that the FEM-DBCI method is fully applicable also using a non-convex truncation boundary Γ_T (see dashed line in Figure 10), which is constituted by a single curve placed at a distance of 1 mm from the conductor surfaces. Due to symmetry reasons, the analysis is restricted to half the system, by imposing a homogeneous Neumann condition on the x -axis. The resulting bounded domain is regularly discretized. The mesh is constituted by 712 s -order triangles and 1483 nodes, of which 127 lie on Γ_T . Having set an end-iteration tolerance of 10^{-4} per cent, convergence is obtained with 13 GMRES iterations. Figures 11 and 12 show the contours of the real and imaginary parts of the magnetic vector potential.

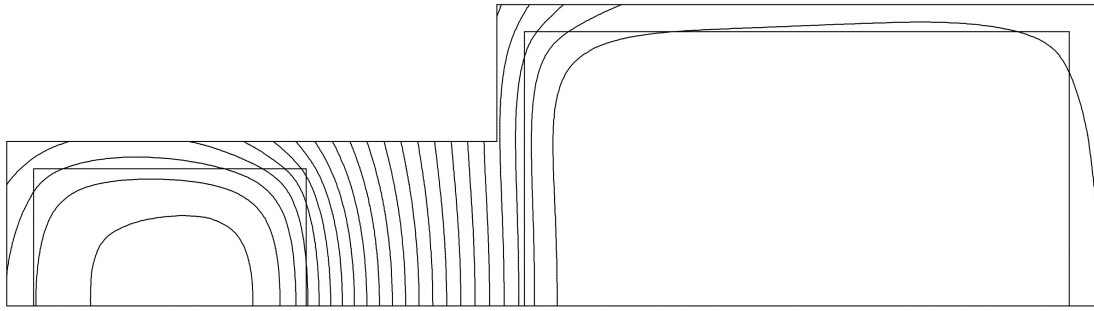


Figure 11. Contours of the real part of the magnetic vector potential.

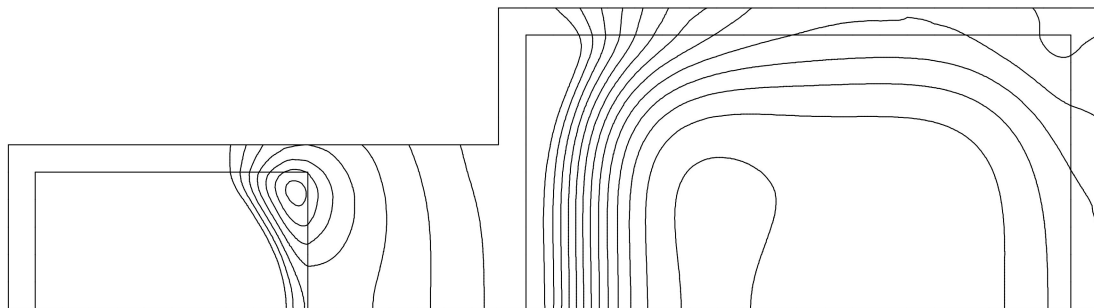


Figure 12. Contours of the imaginary part of the magnetic vector potential.

The solution obtained has been compared with the FEM-BEM one: a mean relative error of about 1.14 per cent is pointed out in the conductors, but the CPU time increases of about 55 per cent.

7. Conclusions

In this paper, a particular use of the hybrid FEM-DBCI method has been described for the solution of a variety of open-boundary electromagnetic problems, such as electrostatic and time-harmonic skin effect ones. In the proposed method, the surface of the integral equation is selected in the middle of the more external layer of finite elements, very near to the truncation boundary. This method leads to accurate numerical results similar to those obtained with the FEM-BEM, but with lower computing times.

For this reason, we can conclude that FEM-DBCI appears to be more appropriate for FEM analyses requiring short computing times, such as in the stochastic optimization of electromagnetic devices. In these applications, generally, several thousands of FEM analyses must be performed to reach satisfactory results [38,39]. On the contrary, FEM-BEM appears more appropriate when high accuracies are required in a single computation.

However, all the hybrid methods suffer from the complexity of the integral equation, which naturally is quadratic. Then, for real industry applications in 3D, it is important to reduce this complexity at the price of adding further approximation to the basic integral equation. In such a perspective, in addition to the well-known fast multipole method (FMM) [40,41], recently the use of H- and H²-matrices seems to be highly promising [42].

The FEM-DBCI method and the non-standard FEM-BEM one used in this paper have been implemented in ELF_{IN}, a large FEM code developed by the authors for scientific research [43].

Author Contributions: Conceptualization, G.A., S.A. and N.S.; methodology, S.A.; software, S.A., S.A.R. and N.S.; All authors have read and agreed to the published version of the manuscript.

Funding: This paper has been partially supported by the Italian Ministry for University and Research (MUR).

Institutional Review Board Statement: Not applicable.

Informed Consent Statement: Not applicable.

Conflicts of Interest: The authors declare no conflict of interest.

References

1. Silvester, P.P.; Ferrari, R.L. *Finite Elements for Electrical Engineers*; Cambridge University Press: Cambridge, UK, 1996.
2. Jin, J. *The Finite Element Method in Electromagnetics*; John Wiley & Sons: New York, NY, USA, 2002.
3. Chen, Q.; Konrad, A. A review of finite element open boundary techniques for static and quasi-static electromagnetic field problems. *IEEE Trans. Magn.* **1997**, *33*, 663–676. [[CrossRef](#)]
4. Lowther, D.A.; Freeman, E.M.; Forghani, B. A sparse matrix open boundary method for finite element analysis. *IEEE Trans. Magn.* **1989**, *25*, 2810–2812. [[CrossRef](#)]
5. Imhoff, J.F.; Meunier, G.; Sabonnadiere, J.C. Finite element modeling of open boundary problems. *IEEE Trans. Magn.* **1990**, *26*, 588–591. [[CrossRef](#)]
6. Bettess, P. Infinite element. *Int. J. Numer. Methods Eng.* **1977**, *11*, 53–64. [[CrossRef](#)]
7. Chen, Q.; Konrad, A.; Biringier, P.P. Computation of three-dimensional unbounded eddy current problems using asymptotic boundary conditions. *IEEE Trans. Magn.* **1995**, *31*, 1348–1351. [[CrossRef](#)]
8. Engquist, B.; Majda, A. Absorbing boundary conditions for the numerical simulation of waves. *Math. Comput.* **1977**, *31*, 629–651. [[CrossRef](#)]
9. Bayliss, A.; Gunzburger, M.; Turkel, E. Boundary conditions for the numerical solution of elliptic equations in exterior regions. *SIAM J. Appl. Math.* **1982**, *42*, 430–451. [[CrossRef](#)]
10. Berenger, J.-P. A perfectly matched layer for the absorption of electromagnetic waves. *J. Comput. Phys.* **1994**, *114*, 185–200. [[CrossRef](#)]
11. Aiello, G.; Alfonzetti, S.; Coco, S. Charge iteration: A procedure for the finite element computation of unbounded electrical fields. *Int. J. Numer. Methods Eng.* **1994**, *37*, 4147–4166. [[CrossRef](#)]
12. Aiello, G.; Alfonzetti, S.; Borzì, G. A generalized minimal residual acceleration of the charge iteration procedure. *J. Phys. III* **1997**, *7*, 1955–1966. [[CrossRef](#)]
13. Aiello, G.; Alfonzetti, S.; Rizzo, S.A.; Salerno, N. FEM-DBCI solution of open-boundary electrostatic problems in the presence of floating potential conductors. *IEEE Trans. Magn.* **2015**, *52*, 1–4. [[CrossRef](#)]
14. Aiello, G.; Alfonzetti, S.; Coco, S.; Salerno, N. Finite element iterative solution to skin effect problems in open boundaries. *Int. J. Numer. Model.* **1996**, *9*, 125–143. [[CrossRef](#)]
15. Aiello, G.; Alfonzetti, S.; Borzì, G.; Salerno, N. An improved solution scheme for open-boundary skin effect problems. *IEEE Trans. Magn.* **2001**, *37*, 3474–3477. [[CrossRef](#)]
16. Aiello, G.; Alfonzetti, S.; Dilettoso, E. Finite element solution of eddy current problems in unbounded domains by means of the hybrid FEM–DBCI method. *IEEE Trans. Magn.* **2003**, *39*, 1409–1412. [[CrossRef](#)]
17. Aiello, G.; Alfonzetti, S.; Salerno, N. Solution of skin-effect problems by means of the hybrid SDBCI method. *COMPEL* **2014**, *33*, 1935–1949. [[CrossRef](#)]
18. Aiello, G.; Alfonzetti, S.; Rizzo, S.A.; Salerno, N. Eddy Current Computation by the FEM-SDBCI Method. *IEEE Trans. Magn.* **2015**, *52*, 1–4. [[CrossRef](#)]
19. Brebbia, C.A.; Telles, J.C.F.; Wrobel, L. *Boundary Element Technique*; Springer: Berlin/Heidelberg, Germany, 1984.
20. Alfonzetti, S.; Salerno, N. A non-standard family of boundary elements for the hybrid FEM-BEM method. *IEEE Trans. Magn.* **2009**, *45*, 1312–1315. [[CrossRef](#)]
21. Yuan, X.; Lynch, D.R.; Strohbehn, J.W. Coupling the finite element and moment methods for electromagnetic scattering from inhomogeneous objects. *IEEE Trans. Antennas Propag.* **1990**, *38*, 386–393. [[CrossRef](#)]
22. Alfonzetti, S.; Borzì, G.; Salerno, N. Iteratively-improved Robin boundary conditions for the finite element solution of scattering problems in unbounded domains. *Int. J. Numer. Methods Eng.* **1998**, *42*, 601–629. [[CrossRef](#)]
23. Alfonzetti, S.; Borzì, G. Finite element solution to electromagnetic scattering problems by means of the Robin boundary condition iteration method. *IEEE Trans. Antennas Propag.* **2002**, *50*, 132–140. [[CrossRef](#)]
24. Alfonzetti, S.; Borzì, G.; Salerno, N. Electromagnetic scattering computation by means of the hybrid FEM-SRBCI method. *IEEE Trans. Magn.* **2015**, *51*, 7401504. [[CrossRef](#)]
25. Liu, J.; Jin, J.M. A novel hybridization of higher order finite element and boundary integral methods for electromagnetic scattering. *IEEE Trans. Antennas Propag.* **2001**, *50*, 132–140.
26. Aiello, G.; Alfonzetti, S.; Dilettoso, E.; Salerno, N. Improving the accuracy of the integral equation in the hybrid FEM-DBCI method for open boundary electrostatic problems. *IEEE Trans. Magn.* **2006**, *42*, 579–582. [[CrossRef](#)]
27. Graglia, R.D. Static and dynamic potential integrals for linearly varying source distributions in two- and three-dimensional problems. *IEEE Trans. Antennas Propag.* **1987**, *35*, 662–669. [[CrossRef](#)]
28. Konrad, A. Integrodifferential finite element formulation of two-dimensional steady-state skin effect problems. *IEEE Trans. Magn.* **1982**, *18*, 284–292. [[CrossRef](#)]
29. Golub, G.H.; van Loan, C.F. *Matrix Computations*; Johns Hopkins University Press: Baltimore, MD, USA, 1996.
30. Aiello, G.; Alfonzetti, S.; Coco, S.; Salerno, N. A theoretical study of charge iteration. *COMPEL* **1996**, *15*, 22–46. [[CrossRef](#)]

31. Aiello, G.; Alfonzetti, S.; Coco, S.; Salerno, N. Overrelaxing the charge iteration procedure. *IEEE Trans. Magn.* **1996**, *32*, 694–697. [[CrossRef](#)]
32. Saad, Y.; Schultz, M.H. GMRES: A generalized minimal residual algorithm for solving nonsymmetric linear systems. *SIAM J. Sci. Stat. Comput.* **1986**, *7*, 856–869. [[CrossRef](#)]
33. Aiello, G.; Alfonzetti, S.; Salerno, N. Solution of skin effect problems by means of the DBCI-GMRES method. *COMPEL* **2002**, *21*, 474–475.
34. Aiello, G.; Alfonzetti, S.; Borzì, G.; Dilettoso, E.; Salerno, N. A GMRES iterative solution of FEM-BEM global systems in skin effect problems. *COMPEL* **2008**, *27*, 1286–1295. [[CrossRef](#)]
35. Aiello, G.; Alfonzetti, S.; Borzì, G.; Rizzo, S.A.; Salerno, N. A comparison between hybrid methods: FEM-BEM versus FEM-DBCI. *COMPEL* **2013**, *32*, 1900–1920. [[CrossRef](#)]
36. Durand, E. *Electrostatique*; Masson Editeur: Paris, France, 1968.
37. Mascagni, M.; Simonov, N.A. The random walk on the boundary method for calculating capacitance. *J. Comput. Phys.* **2004**, *195*, 465–473. [[CrossRef](#)]
38. Alfonzetti, S.; Dilettoso, E.; Salerno, N. Simulated annealing with restarts for the optimization of electromagnetic devices. *IEEE Trans. Magn.* **2006**, *42*, 1115–1118. [[CrossRef](#)]
39. Aiello, G.; Rizzo, S.A.; Alfonzetti, S.; Salerno, N. Optimization of the shape of an induction heating device in the presence of skin effect in the coils. *COMPEL* **2019**, *39*, 525–531. [[CrossRef](#)]
40. Rokhlin, V. Rapid solution of integral equations of classical potential theory. *J. Comput. Phys.* **1985**, *60*, 187–207. [[CrossRef](#)]
41. Engheta, N.; Murphy, W.D.; Rokhlin, V.; Vassiliou, M. The fast multipole method for electromagnetic scattering computation. *IEEE Trans. Antennas Propag.* **1992**, *40*, 634–641. [[CrossRef](#)]
42. Hackbusch, W. *Hierarchical Matrices: Algorithms and Analysis*; Springer Series in Computational Mathematics; Springer: Berlin/Heidelberg, Germany, 2015. [[CrossRef](#)]
43. Aiello, G.; Alfonzetti, S.; Borzì, G.; Salerno, N. An overview of the ELFIN code for finite element research in electrical engineering. In *Software for Electrical Engineering Analysis and Design*; Konrad, A., Brebbia, C.A., Eds.; WIT Press: Southampton, UK, 1999.